

Near-Field XL-MIMO Systems with Sparse UPAs

Xianzhe Chen, Hong Ren, *Member, IEEE*, Cunhua Pan, *Senior Member, IEEE*

Abstract—This paper investigates a downlink near-field extremely large-scale multiple-input multiple-output (XL-MIMO) communication system with sparse uniform planar arrays (UPAs). Based on the Green’s function-based channel model, the paper focuses on the power distribution of the arrived signal near the focused point of the transmit sparse UPA. In the vicinity of the focused point, along the x-axis and z-axis directions, closed-form expressions for the power distributions are derived. Based on that, expressions for the width and length of the main lobe are obtained in closed form, both of which decrease as the antenna spacing increases. Furthermore, the paper introduces a crucial constraint on system parameters, under which effective degrees-of-freedom (EDoF) of XL-MIMO systems with sparse UPAs can be precisely estimated. Then, the paper proposes an algorithm to obtain a closed-form expression, which can estimate EDoF with high accuracy and low computational complexity. The numerical results verifies the correctness of the main results of this paper. Furthermore, the numerical results reveals the improvement in the performance of XL-MIMO systems with the use of sparse UPAs.

Index Terms—Extremely large-scale MIMO, sparse uniform planar array, antenna spacing, main and side lobes, effective degrees-of-freedom (EDoF)

I. INTRODUCTION

Massive multiple-input multiple-output (MIMO) has been a key technology in fifth-generation (5G) communications for its merits in terms of spectral efficiency, energy efficiency and power control [1]–[5]. However, future sixth-generation (6G) communications set higher requirements, including ultra-reliability, high capacity densities, extremely low-latency and low-energy consumption. To meet these requirements, extremely large-scale MIMO (XL-MIMO), as an advanced evolution of massive MIMO, has garnered significant attention in recent research [6]–[9]. Compared to conventional massive MIMO, XL-MIMO employs an order-of-magnitude larger number of antennas to achieve exceptionally high spectral efficiency. The significantly increased number of antennas not only expands the array size but also shifts the system’s operational environment from the traditional far-field region to the near-field region. As a result, new channel characteristics appears such as the spherical wavefront, spatial non-stationarity and so on [10]–[13].

The advantages introduced by the spherical wavefront in near-field XL-MIMO systems have garnered significant attention from researchers. In contrast to conventional far-field channels, where the planar wavefront results in highly restricted degrees-of-freedom (DoF) due to a single spatial angle [14], the near-field scenario offers a notable improvement. When the spherical wavefront is accounted for, the spatial

angles vary across the entire transmit/receive array, leading to a substantial increase in DoF and, consequently, a significant enhancement in channel capacity.

Therefore, it is crucial to investigate the DoF in near-field XL-MIMO systems. Given that channel capacity largely depends on the orthogonal sub-channels with significant singular values [15], extensive research has focused on the effective DoF (EDoF), defined as the number of significant singular values in the channel matrix. In [16], a concise estimation of EDoF was proposed based on the maximum number of intensity fringes. Utilizing arguments from two-dimensional (2D) sampling theory, approximate expressions for the EDoF of communication channels between a large intelligent surface (LIS) and a small intelligent surface (SIS) were derived in [17]. The EDoF of systems with two non-parallel arrays and its impact on channel capacity were analyzed in [18]. In the context of free-space MIMO systems, [19] investigated the EDoF, which was computed using the channel matrix. Additionally, [20] derived closed-form expressions for the EDoF in near-field XL-MIMO systems by leveraging Green’s function-based channels.

Based on the aforementioned studies, the channel capacity of XL-MIMO systems can be significantly enhanced by increasing the effective degrees of freedom (EDoF). The EDoF can be increased by either augmenting the number of antennas [19] or reducing the distance between the transmit and receive arrays [18]. However, these methods offer only limited improvements in EDoF, meaning that substantial EDoF gains can only be realized with an excessively large number of antennas or by positioning the transmit and receive arrays extremely close to each other, both of which are impractical solutions. To address that, our work [21] focused on the impact of antenna spacing on EDoF, which showed that EDoF can be largely increase as the antenna spacing increases, indicating an outstanding advantage in using sparse arrays in near-field XL-MIMO systems.

The potential of achieving high EDoF has motivated us to explore additional benefits of employing sparse arrays in near-field XL-MIMO systems. It is worth noting that sparse arrays will give rise to unintended side lobes, which are additional dominant lobes with intensities comparable to the main lobe, bringing extra inter-user interference to communication systems. Although the width of the main lobe and side lobes can be reduced by the increased antenna spacing [22], the interference still poses a significant challenge in conventional far-field communication systems. Thus, effective techniques for suppressing side lobes are needed when using sparse arrays in far-field systems [23]–[25].

In contrast, near-field XL-MIMO communication systems can offer notable advantages in reducing the area of the main lobe and side lobes through the increased antenna spacing. In

(Corresponding author: Cunhua Pan)

X. Chen, H. Ren, C. Pan and Jiangzhou Wang are with the National Mobile Communications Research Laboratory, Southeast University, Nanjing 210096, China (e-mail: chen.xianzhe, hren, cpan, j.z.wang@seu.edu.cn).

[26], the inter-user interference was investigated considering a reduced width of the lobes in XL-MIMO systems with sparse uniform linear arrays (ULAs). A XL-MIMO system with modular ULA was studied in [27], which indicated the reduction in both width and length of the lobes in XL-MIMO systems with sparse ULAs. This result was also illustrated in [9]. In [28], the authors pointed out that the XL-MIMO array has a limited beamfocusing area. These works demonstrate that not only the width but also the length of the lobes are reduced when sparse arrays are used in near-field XL-MIMO systems. It is because the increased antenna spacing in sparse arrays make the variation of spatial angles caused by the near-field spherical wavefront more drastic across the entire array, making the phase of the signals sensitive to the direction perpendicular to the array. Thus, sparse arrays in the near-field systems can inherently suppress the interference lobes, particularly when the antenna spacing is large, which presents a promising solution to address the challenge of severe interference appeared in far-field scenarios.

Motivated by these, we decide to investigate a near-field XL-MIMO communication system with sparse arrays in this paper. It is noted that few works in existing literature have analyzed the variation of the lobes in XL-MIMO system with sparse uniform planar arrays (UPAs), and closed-form expressions for the width and length of the lobes are urgently needed to investigate their characters versus the antenna spacing. Therefore, we will focus on the width and length of the lobes with sparse UPAs, and derive their closed-form expressions to fulfill the the research gap in this area. Based on that, we can precisely characterize the variation of the lobes versus antenna spacing. Furthermore, an EDoF estimation method is crucial since near-field XL-MIMO systems with sparse UPAs are expected to have a high EDoF. Noting that the existing EDoF estimation methods are whether with limited accuracy [16] or with high computational complexity [20], we will propose an algorithm to obtain a closed-form expression for EDoF in sparse UPAs with high accuracy and low computational complexity. The main contributions of this paper are summarized as follows:

- We investigate a downlink near-field XL-MIMO communication system with sparse UPAs. We derive a closed-form expression for the power distribution of the arrived signal in x -axis around the focused point \mathbf{r}_0 . Then a closed-form expression for the width of the main lobe is derived. It shows that the width of the main lobe decreases as the antenna spacing increases.
- We derive a closed-form expression for the power distribution of the arrived signal in z -axis around the focused point \mathbf{r}_0 . Based on that, a closed-form expression for the length of the main lobe is derived. It illustrates that the length of the main lobe decreases as the antenna spacing increases, which differs significantly from the case of sparse arrays in far-field systems.
- We introduce a critical constraint on the system parameters under which the EDoF of XL-MIMO systems with sparse UPAs can be precisely estimated. Based on that, we propose an algorithm to obtain a closed-form expression for EDoF, which can estimates EDoF with

high accuracy and low computational complexity.

- Simulation results are provided to verify the correctness of the main results of this paper. We further reveal that in XL-MIMO systems with sparse UPAs, the total interference caused by the main lobe and side lobes decreases as the antenna spacing increases, which indicates a promising feasibility of using sparse arrays in XL-MIMO systems.

The remainder of this paper is organized as follows: Section II introduces a downlink near-field XL-MIMO communication system equipped with a sparse UPA. Section III derives closed-form expressions for the power distribution of the arrived signal near the focused point, and obtains the expressions for the width and length of the main lobe. Section IV proposes an algorithm to obtain a closed-form expression for EDoF. Section V provides numerical results to verified the main results of this paper. Section VI gives a brief conclusion of this paper.

Notations: In this paper, scalars, vectors and matrices are respectively denoted by lower case letters, bold lower case letters and bold upper case letters. The matrix inverse, conjugate-transpose, transpose and conjugate operations are respectively denoted by the superscripts $(\cdot)^{-1}$, $(\cdot)^H$, $(\cdot)^T$ and $(\cdot)^*$. We use $\text{tr}(\cdot)$, $\|\cdot\|$ and $\mathbb{E}\{\cdot\}$ to denote trace, Euclidean 2-norm and the expectation operations, respectively.

II. SYSTEM MODEL

Consider a downlink near-field XL-MIMO communication system as depicted in Fig. 1, where a sparse UPA is deployed at the base station (BS) with the size of $\sqrt{N} \times \sqrt{N}$ to transmit signals to users.

By designing the precoding vector, the XL-MIMO array can focus on a given point $\mathbf{r}_0(0, 0, L)$. Assuming that the XL-MIMO array transmits data symbol s to \mathbf{r}_0 with the same transmit power of $\frac{P}{N}$ for each antenna, the arrived signal f_0 at \mathbf{r}_0 from the BS can be expressed as

$$f_0 = \sum_{n=1}^{\sqrt{N}} \sum_{m=1}^{\sqrt{N}} t_{n,m}^0 e^{i\theta_{n,m}^0} s, \quad (1)$$

where the index (n, m) represents the relative position for antennas in the UPA, as shown in Fig. 1. Scalar $t_{n,m}^0$ represents the Green's Function-based channel coefficient between the UPA and position \mathbf{r}_0 , which is widely used in near-field XL-MIMO systems, given by

$$\begin{aligned} t_{n,m}^0 &= -\frac{\exp(ik|(\bar{x}_n, \bar{y}_m, 0) - (0, 0, L)|)}{4\pi|(\bar{x}_n, \bar{y}_m, 0) - (0, 0, L)|} \\ &= -\frac{\exp\left(ik\sqrt{\bar{x}_n^2 + \bar{y}_m^2 + L^2}\right)}{4\pi\sqrt{\bar{x}_n^2 + \bar{y}_m^2 + L^2}} \approx -\frac{e^{i2\pi\sqrt{\bar{x}_n^2 + \bar{y}_m^2 + L^2}}}{4\pi L}, \end{aligned} \quad (2)$$

where \bar{x}_n and \bar{y}_m are respectively given by

$$\begin{aligned} \bar{x}_n &= \left(n - \frac{\sqrt{N} + 1}{2}\right) d, \\ \bar{y}_m &= \left(m - \frac{\sqrt{N} + 1}{2}\right) d, \end{aligned} \quad (3)$$

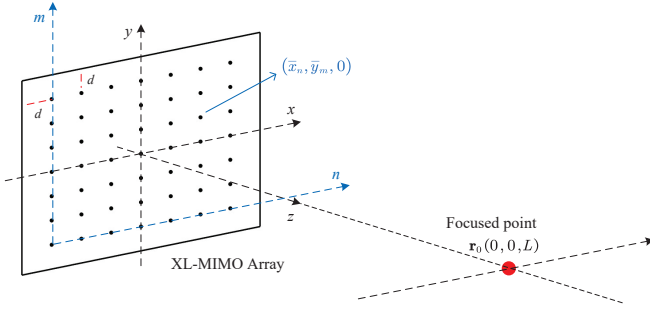


Fig. 1. System Model

with d representing the antenna spacing. The approximation in (2) holds due to the fact that the power variations over arrays are negligible in radiative near field compared to the phase variations [28]. Scalar $\theta_{n,m}^0$ is the phase shift imposed on antenna (n, m) , which is determined by the precoding vector to make the UPA focus on \mathbf{r}_0 . Then, the power of f_0 can be expressed as

$$P_0 = \frac{P}{N} \left| \sum_{n=1}^{\sqrt{N}} \sum_{m=1}^{\sqrt{N}} t_{n,m}^0 e^{i\theta_{n,m}^0} \right|^2$$

$$= \frac{P}{N(4\pi L)^2} \left| \sum_{n=1}^{\sqrt{N}} \sum_{m=1}^{\sqrt{N}} e^{i\frac{2\pi}{\lambda} \sqrt{\bar{x}_n^2 + \bar{y}_m^2 + L^2}} e^{i\theta_{n,m}^0} \right|^2. \quad (4)$$

Since the UPA focuses on \mathbf{r}_0 , P_0 is expected to be maximized, and thus we have

$$\theta_{n,m}^0 = -\frac{2\pi}{\lambda} \sqrt{\bar{x}_n^2 + \bar{y}_m^2 + L^2}. \quad (5)$$

Equation (5) gives the expression for the phase shift $\theta_{n,m}^0$ imposed on antenna (n, m) to make the UPA focus on \mathbf{r}_0 .

III. STRONG INTERFERENCE REGION FOR SPARSE ARRAYS

When the XL-MIMO system with sparse UPAs transmits signal to the user at the focused point \mathbf{r}_0 , severe interference will be imposed on the other users in the main lobe and side lobes inevitably, as shown in Fig. 2. These regions, where non-target users will receive severe interference, are defined as the severe interference region.

The conventional collected array adopts half wavelength antenna spacing to avoid side lobes, and thus improves the system performance due to the reduction of the area of the severe interference region. On the contrary, the sparse array with antenna spacing larger than half wavelength has a larger area of the severe interference region due to the side lobes, resulting in a decrease in the performance of the systems operating in the far-field region.

However, when considering the near-field region, as the spherical wavefront is taken into consideration, we find that XL-MIMO systems can decrease the area of the severe interference region by increasing the antenna spacing, bringing an improvement in system performance, which will be further discussed in the follow subsections.

A. Lobe Width of Main Lobe in x -Axis

As the situation in the far-field case, the width of the lobes in the near-field case will decrease as the antenna spacing increases, resulting to a decrease of the area of the severe interference region. Without loss of generality, we consider the width of the main lobe in this subsection.

To derive the width of the main lobe, we consider the signal f_1 arrived at $\mathbf{r}_1(\bar{d}, 0, L)$ which has a displacement of \bar{d} in the x -axis direction relative to the focused position \mathbf{r}_0 . The following theorem derives a closed-form expression for the power of f_1 .

Theorem 1: When the XL-MIMO array focuses on $\mathbf{r}_0(0, 0, L)$, the power P_1 of the signal f_1 arrived at $\mathbf{r}_1(\bar{d}, 0, L)$ can be approximated as

$$P_1 \approx \frac{PN}{(4\pi L)^2} \frac{\sin^2 c^2 \left(\frac{d\bar{d}\sqrt{N}}{\lambda L} \right)}{\sin^2 c^2 \left(\frac{d\bar{d}}{\lambda L} \right)}. \quad (6)$$

Proof: Please refer to Appendix A. ■

Theorem 1 illustrates the power distribution of the arrived signal in x -axis around the focused point \mathbf{r}_0 . It is noted from Theorem 1 that P_1 satisfies a sinc-like function relative to \bar{d} . Due to the sinc-like characteristic, P_1 will drop to zero when \bar{d} increases from zero to its first zero-point value. On other words, when P_1 is at its first zero point, \bar{d} can represent the width of the main lobe, which means that

$$\frac{d\bar{d}\sqrt{N}}{\lambda L} = 1 \Rightarrow \bar{d} = \frac{\lambda L}{d\sqrt{N}}. \quad (7)$$

Equation (7) gives a closed-form expression for the width of the main lobe in near-field XL-MIMO systems with sparse UPAs. It is readily observed that the width of the main lobe is inversely proportional to the antenna spacing d and is proportional to the inverse square root of the number of antennas N .

It is worth noting that in the far-field case, since the parameters satisfy $\frac{\bar{d}}{L} \approx \sin \theta$, where θ represents the deviation angle from z_+ -axis, the angle width of the main lobe can be obtained from (7) as

$$\sin \theta = \frac{\lambda}{d\sqrt{N}}, \quad (8)$$

which is consistent with the results of [22], verifying the correctness of our derivation. Additionally, it is observed that equations (7) and (8) exhibit similar forms, which indicates that in both far-field and near-field scenarios, the influence of the antenna spacing d on the width of the main lobe is similar.

B. Lobe Length of Main Lobe in z -Axis

Different from the far-field case, the length of the lobes in the near-field case will also decrease as the antenna spacing increases, which further reduces the area of the severe interference region. Similarly, without loss of generality, we consider the length of the main lobe in this subsection.

To investigate the length of the main lobe, we pay attention to the signal f_2 arrived at $\mathbf{r}_2(0, 0, L + \bar{L})$ which has a displacement of \bar{L} in the z -axis direction relative to the focused

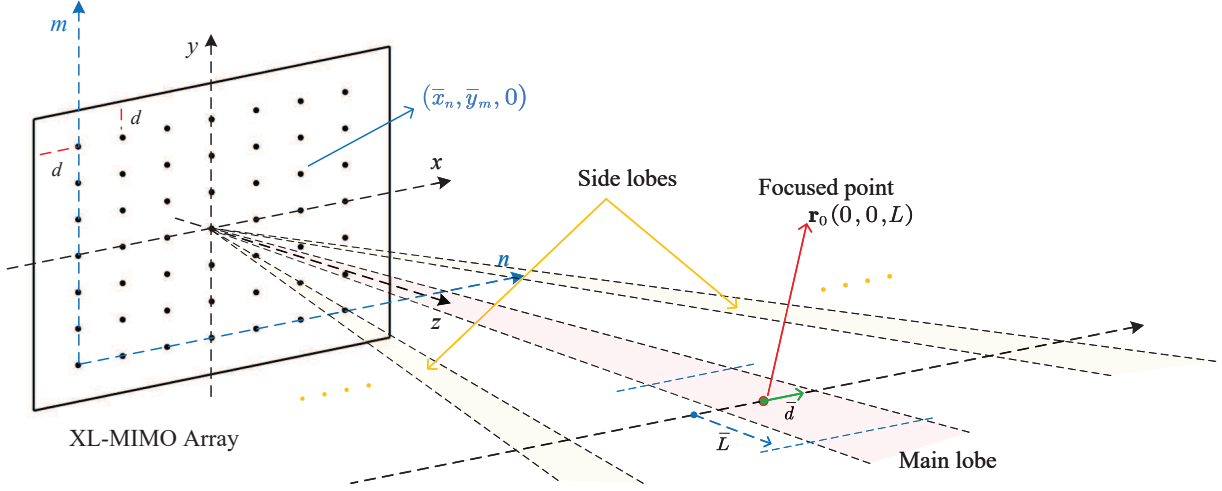


Fig. 2. Severe interference region for sparse UPAs

position \mathbf{r}_0 . Then, we derive a closed-form expression for the power of f_2 in the following theorem.

Theorem 2: When the XL-MIMO array focuses on $\mathbf{r}_0(0,0,L)$, the power P_2 of the signal f_2 arrived at $\mathbf{r}_2(0,0,L+\bar{L})$ can be approximated as

$$P_2 \approx \frac{P}{(4\pi(L+\bar{L}))^2} \rho_2, \quad (9)$$

where ρ_2 is expressed as

$$\rho_2 \approx \begin{cases} \frac{(\sqrt{N}-1)^4}{N} \cdot \frac{1}{b^4} (C^2(b) + S^2(b))^2, & \eta \neq 0 \\ \frac{(\sqrt{N}-1)^4}{N}, & \eta = 0 \end{cases}, \quad (10)$$

with parameters given by

$$\begin{aligned} b &= \sqrt{|A\eta|} \cdot \frac{\sqrt{N}-1}{2}, \\ A &= \frac{\pi d^2}{\lambda L}, \\ \eta &= \frac{\bar{L}}{L+\bar{L}}. \end{aligned} \quad (11)$$

Functions $C(\cdot)$ and $S(\cdot)$ are Fresnel integrals, respectively expressed as

$$\begin{aligned} C(x) &= \int_0^x \cos\left(\frac{\pi}{2}t^2\right) dt, \\ S(x) &= \int_0^x \sin\left(\frac{\pi}{2}t^2\right) dt. \end{aligned} \quad (12)$$

Proof: Please refer to Appendix B. ■

Theorem 2 depicts the power distribution of the arrived signal in z -axis around the focused point \mathbf{r}_0 . However, due to the complexity of the expression in (10), useful information regarding the length of the main lobe cannot be directly obtained. To address that, we investigate the characteristic of ρ_2 in the following corollary.

Corollary 1: When b is close to zero, the function ρ_2 given by Eq. (10) will decrease rapidly and monotonically as b

increases. When b becomes large, ρ_2 will fluctuate within a limited range as b grows.

Proof: Please refer to Appendix C. ■

Corollary 1 indicates that ρ_2 has a main lobe in the vicinity of $b = 0^+$ with its peak located at $b = 0$, which, from (9), corresponds to the main lobe of the arrived signal in z -axis centered at $\mathbf{r}_0(0,0,L)$. Furthermore, the width of the lobe can be represented by the local minimum point b_{\min} closest to $b = 0$, which can be obtained by Algorithm 1 as

$$b_{\min} = 1.9111. \quad (13)$$

Since b is a monotonically increasing function of $|\eta|$, the length of the main lobe of the arrived signal in z -axis centered at $\mathbf{r}_0(0,0,L)$ can be represented by

$$|\eta| = \frac{4b_{\min}^2}{(\sqrt{N}-1)^2} \cdot \frac{\lambda L}{\pi d^2}. \quad (14)$$

From (11), we can further obtain the length of the main lobe in z_+ -axis and z_- -axis respectively as

$$\begin{aligned} \bar{L}_+ &= \frac{L}{\frac{\pi d^2(\sqrt{N}-1)^2}{4b_{\min}^2 \lambda L} - 1}, \\ \bar{L}_- &= \frac{-L}{\frac{\pi d^2(\sqrt{N}-1)^2}{4b_{\min}^2 \lambda L} + 1}. \end{aligned} \quad (15)$$

Equation (15) provides closed-form expressions for the length of the main lobe in near-field XL-MIMO systems with sparse UPAs.

It should be aware from (15) that, to ensure the main lobe of sparse UPAs concentrates at the focused point \mathbf{r}_0 along the z -axis, the following constraint

$$\bar{L}_+ > 0 \Rightarrow d > \frac{2b_{\min}}{\sqrt{N}-1} \sqrt{\frac{\lambda L}{\pi}} \approx 2b_{\min} \sqrt{\frac{\lambda L}{\pi N}} \quad (16)$$

must be met. This indicates that the phenomenon of the main lobe length reduction only occurs when the antenna spacing d in a sparse UPA exceeds a certain threshold given by (16).

Algorithm 1 Finding the Local Minimum Point

```

1: Input: Initial value  $b = 0.0001$ , step size  $\Delta b = 0.001$ ,
   number of antennas  $N$ 
2: Input: Function  $\rho_2(b, N)$ 
3:  $\rho_{\text{prev}} = \rho_2(b, N)$ ;
4: while true do
5:    $b_{\text{new}} = b + \Delta b$ ;
6:    $\rho_{\text{new}} = \rho_2(b_{\text{new}}, N)$ ;
7:   if  $\rho_{\text{new}} < \rho_{\text{prev}}$  then
8:      $b = b_{\text{new}}$ ;
9:      $\rho_{\text{prev}} = \rho_{\text{new}}$ ;
10:  else
11:    Output  $b_{\text{min}} = b$  as a local minimum point
12:    Stop
13:  end if
14: end while
15: Return: Local minimum point  $b_{\text{min}}$ 

```

The reason can be found in (35) and (36) in Appendix B. A small value of d results in a correspondingly small value of A in (36), where A is the factor governing the signal phase variation with respect to \bar{L} . As a result, the phase variation induced by changes in \bar{L} causes minimal fluctuations in ρ_2 of (35). This leads to the dominance of the path loss factor $\frac{P}{(4\pi(L+\bar{L}))^2}$ in P_2 of (9), preventing the signal energy from being concentrated at the focused point \mathbf{r}_0 along the z -axis.

On the other hand, when the antenna spacing exceeds the constraint (16), it is readily observed from (15) that the length of the main lobe decreases as the antenna spacing increases.

In (7) and (15), we respectively provide the closed-form expressions for the width and length of the main lobe of a near-field XL-MIMO system with sparse UPAs, illustrating that both the width and length of the main lobe will decrease as the antenna spacing d increases. It is worth noting that this result is also suitable for the side lobes, since they are caused by the periodic variation of the phase. Therefore, the area of the severe interference region can be largely reduced by increasing the antenna spacing, and thus the inter-user interference in multi-user scenarios can be significantly reduced. This indicates a promising feasibility of using sparse arrays in XL-MIMO systems.

IV. EDOF FOR SPARSE ARRAYS

A critical advantage of XL-MIMO is that it can largely improve the EDoF of communication systems due to the spherical wavefront in near-field. However, in our previous work [21], we found that the increase of EDoF is actually limited in conventional collected arrays ($d = \lambda/2$), while the sparse array can largely improve the EDoF. This finding indicates an outstanding benefit of using sparse arrays in XL-MIMO systems.

A. Advantage of Sparse Arrays in EDoF

In Fig. 3, we directly show the advantage of sparse arrays in EDoF. Two systems are considered, one is equipped with collected arrays ($d = \lambda/2$), and the other is equipped with

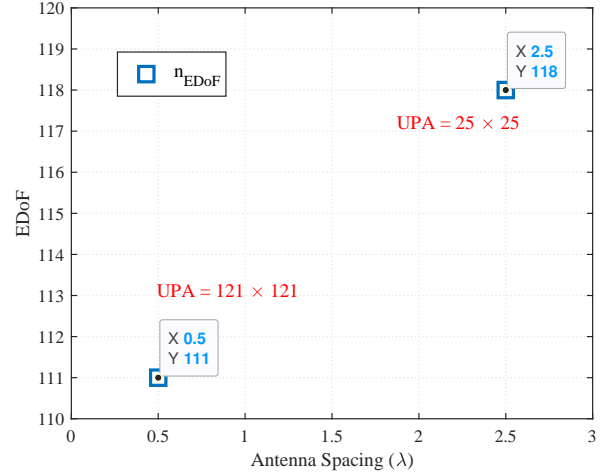


Fig. 3. EDoF comparison

sparse arrays ($d = 2.5\lambda$). The system with collected arrays uses UPAs with the size of 121×121 for transmitting and receiving signals, while the system with sparse arrays uses UPAs with the size of 25×25 , which means UPAs in the two systems have the same physical size. The distance between the transmit and receive UPAs is set as $L = 400\lambda$. It can be observed that the sparse array system with a much lower number of antennas can achieve a higher EDoF than the collected array system, which indicates the outstanding advantage of sparse arrays in increasing EDoF.

B. Existing EDoF Estimation Methods

As XL-MIMO systems can increase EDoF by bringing the communication environment into the near-field region, the methods to estimate EDoF have drawn extensive research attention.

The direct solution to obtain EDoF is to count the number of significant singular values of \mathbf{G} , which is the channel matrix between the transmitter and receiver. This process can be described by

$$n_{\text{EDoF}} = \underset{n}{\operatorname{argmin}} \left\{ f(n) = \sum_{i=1}^n \mu_i^2 \left| \frac{f(n)}{\sum_{i=1}^{n_{\text{EDoF}}} \mu_i^2} \geq 99.9\% \right. \right\}, \quad (17)$$

where μ_i represents the i -th largest singular value of \mathbf{G} . It is noted that the direct solution does not give a closed-form expression for EDoF. Besides, μ_i is obtained by the SVD operation, which has a high computational complexity.

One of the widely used method to estimate the EDoF is given by [16]

$$n_{\text{EDoF1}} = \frac{A_S A_R}{\lambda^2 L^2}, \quad (18)$$

where A_S and A_R are the areas of the transmit and receive arrays, respectively. This method provides a concise closed-form expression for EDoF, but its accuracy is limited.

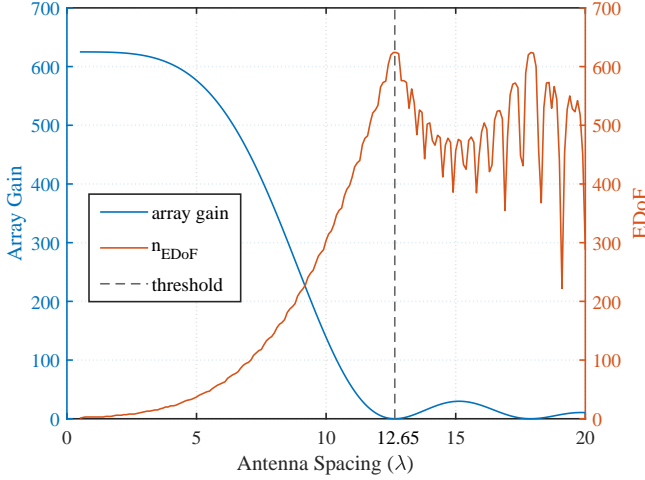


Fig. 4. Relationship between array gain and EDoF

Another method can estimate EDoF providing relatively better accuracy with the closed-form expression given by [19]

$$n_{\text{EDoF}2} = \frac{\text{tr}^2(\mathbf{G}\mathbf{G}^H)}{\|\mathbf{G}\mathbf{G}^H\|_{\text{F}}^2} = \frac{(\sum_i \mu_i^2)^2}{\sum_i \mu_i^4}. \quad (19)$$

However, this estimation method still has the drawback of high computational complexity.

C. EDoF Estimation in Sparse Array Systems

In XL-MIMO systems with sparse arrays, EDoF can be effectively improved. Thus, it is critical to estimate EDoF, especially with a closed-form expression, which is valuable for the system design. However, as is discussed in the previous subsection, the closed-form expressions in existing EDoF estimation methods are whether with limited accuracy or with high computational complexity. To address that, we aim to propose a method in this subsection to obtain a closed-form expression, which can estimate EDoF in sparse array systems with high accuracy and low computational complexity.

In our previous work [21], we illustrated that when the transmit array focuses on one antenna of the receive array, EDoF is maximized when the array gain at the antenna nearest to the focused antenna is minimized. This result can be depicted by Fig. 4. It can be observed that EDoF grows steadily when the array gain drops to its first zero point. After the first zero point of the array gain, EDoF exhibits irregular fluctuations. Therefore, we consider that before the first zero point of the array gain, EDoF can be estimated by performing function fitting using system parameters.

Since the array gain is directly proportional to the power of the arrived signal, P_1 in (6) of Theorem 1 can represent the array gain at the antenna nearest to the focused antenna, when \bar{d} is the antenna spacing of the receive array. Thus, the condition “before the first zero point of the array gain” can be translated as the following constraint

$$\frac{d\bar{d}\sqrt{N}}{\lambda r} < 1, \quad (20)$$

Algorithm 2 Obtain the EDoF Fitting Function

- 1: **INPUT:** Antenna spacing of the transmit array d , antenna spacing of the receive array \bar{d} , the number of transmit antennas N , system operating wavelength λ
- 2: **INPUT:** Range vector of users' angles $\theta \in [\theta_{\min} : \theta_{\text{step}} : \theta_{\max}]$, Range vector of distance between the transmit array and users $\mathbf{r} \in [r_{\min} : r_{\text{step}} : r_{\max}]$
- 3: **if** $\frac{d\bar{d}\sqrt{N}}{\lambda r_{\min}} < 1$ **then**
- 4: **for** $i = 1 : \text{length}(\theta)$ **do**
- 5: **for** $j = 1 : \text{length}(\mathbf{r})$ **do**
- 6: Compute EDoF for the (i, j) element of the EDoF matrix \mathbf{H}_{EDoF} using direct solution (17);
- 7: **end for**
- 8: **end for**
- 9: **else**
- 10: **Print** “Invalid Input”;
- 11: **end if**
- 12: **FITTING PROCESS:**
- 13: Fit the relationship between EDoF matrix \mathbf{H}_{EDoF} and angle vector θ and distance vector \mathbf{L} by MATLAB tools, and obtain the EDoF fitting function $f_{\text{EDoF}}(\theta, r)$;
- 14: **OUTPUT:** EDoF Fitting function $f_{\text{EDoF}}(\theta, r)$

where r is the distance between the transmit array and users.

In practice, it is important to obtain EDoF for users at different positions. Therefore, we are interested in obtaining a closed-form expression for EDoF that relates the position of users. For the case that the distance range of interest between the transmit array and users satisfies the constraint (20), we propose Algorithm 2 to obtain a EDoF fitting function $f_{\text{EDoF}}(\theta, r)$. Then, the closed-form expression $f_{\text{EDoF}}(\theta, r)$ can estimate EDoF of each user with its position information.

Algorithm 2 provides a EDoF fitting function $f_{\text{EDoF}}(\theta, r)$ for users in the XoZ plane, where θ represents the deviation angle of users from z_+ -axis. When the system parameters satisfy the constraint (20), EDoF varies steadily with the system parameters, making the function fitting yield excellent results. Therefore, the EDoF fitting function $f_{\text{EDoF}}(\theta, r)$ is very accuracy. Additionally, $f_{\text{EDoF}}(\theta, r)$ only depends on the users' position parameters θ and r , which indicates that, once the user position is established, the computation of EDoF entails minimal complexity.

V. NUMERICAL RESULTS

In this section, numerical results are provided to verify the main results of this paper and provide more insights. We assume that the XL-MIMO system operates at 30 GHz, i.e., $\lambda = 0.01$ m. A UPA is used for the XL-MIMO system with the size of $N = 35 \times 35$. The UPA is placed in the XoY plane, with its edges parallel to the coordinate axes and the center at $(0, 0, 0)$. Additionally, we assume that the UPA focuses on the point $\mathbf{r}_0(0, 0, L)$.

Fig. 5 and Fig. 6 respectively depicts the power distribution of the arrived signal in x -axis near the focused point \mathbf{r}_0 with $d = 0.5\lambda$ and $d = 10\lambda$, where d is the antenna spacing of the UPA. The blue solid line is based on the real value

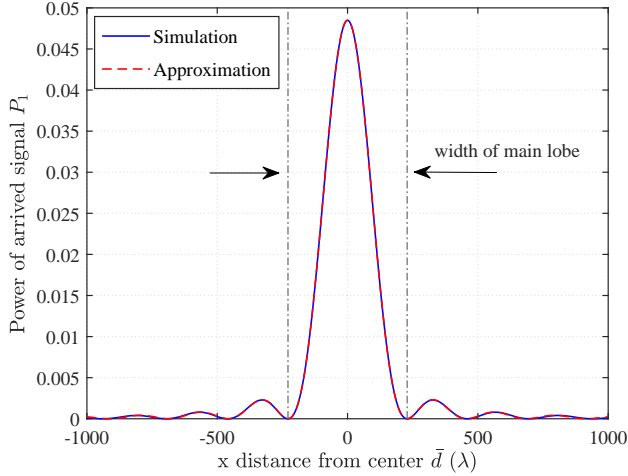


Fig. 5. Power distribution in x -axis with $d = 0.5\lambda$

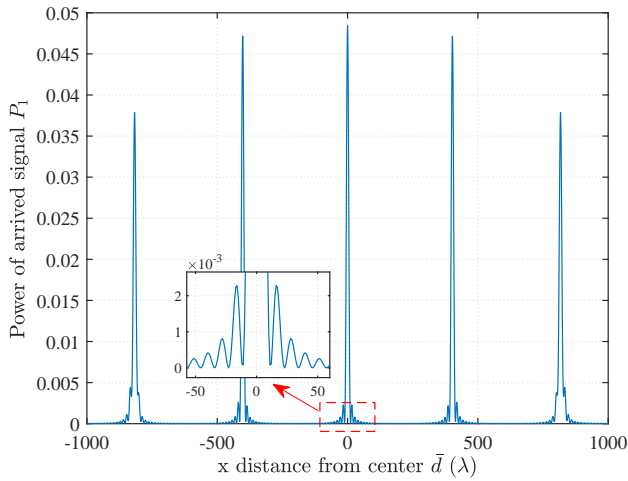


Fig. 6. Power distribution in x -axis with $d = 10\lambda$

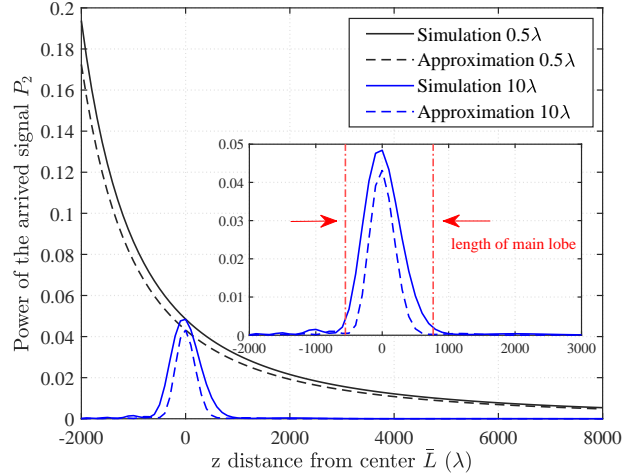


Fig. 7. Power distribution in z -axis with $d = 0.5\lambda$ and $d = 10\lambda$

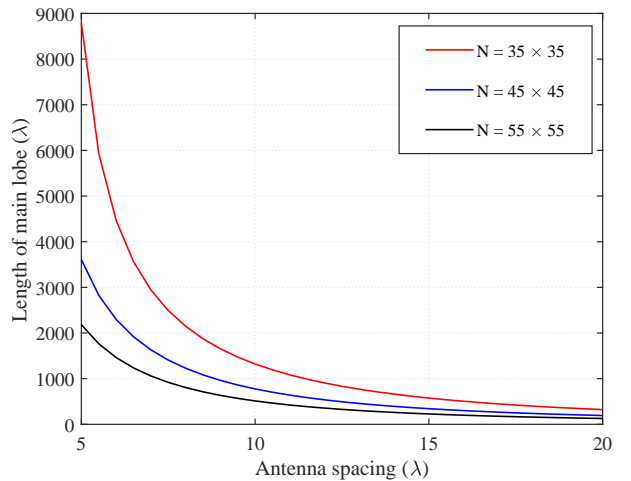


Fig. 8. Length of main lobe in z -axis versus antenna spacing

of the arrived signal, while the red dashed line is based on the approximation given by P_1 in Theorem 1. It is readily to observe that the two line match quite well, which verifies the correctness of Theorem 1. The vertical lines in Fig. 5 are drawn at $x = \pm\bar{d} = \pm\frac{\lambda L}{d\sqrt{N}}$ given by (7). As is observed, these two vertical lines effectively delineate the width of the main lobe, which further supports the result of Theorem 1.

Furthermore, we can find that although the case with $d = 0.5\lambda$ avoids the side lobes, its main lobe has a large width, which increases the area of the severe interference region. This is unfavorable for multi-user communication, as a greater number of non-target users are likely to fall within the region, leading to increased interference. On the other hand, although side lobes are present, the case with $d = 10\lambda$ exhibits a narrow lobe width, which effectively reduces the area of the severe interference region, indicating a potential improvement in system performance.

Fig. 7 illustrates the power distribution of the arrived signal in z -axis near the focused point \mathbf{r}_0 with $d = 0.5\lambda$ and $d = 10\lambda$. The solid lines are based on the real value of the arrived signal,

while the dashed lines are based on the approximation given by P_2 in Theorem 2. It can be observed that the dashed lines well match the solid lines, indicating the correctness of Theorem 2. Two red vertical lines are drawn at $x = \bar{L}_-$ and $x = \bar{L}_+$ based on (15), based on which the length of the main lobe is expressed as

$$\bar{L}_{z\text{length}} = \bar{L}_+ - \bar{L}_-. \quad (21)$$

As is observed in Fig. 7, in the case with $d = 0.5\lambda$, the power of the arrived signal P_2 decreases monotonically with \bar{L} . This can be explained by (35) and (36), which indicate that when the antenna spacing is small, the phase variation induced by \bar{L} is tiny, and accordingly, the signal power variation is negligible. Consequently, the path loss factor $\frac{P}{(4\pi(L+\bar{L}))^2}$ in P_2 of (9) becomes the dominant factor influencing the variation in signal power. This phenomenon results in severe interference for users located between the transmit array and the target user. On the other hand, when the antenna spacing grows, it is observed from the case with $d = 10\lambda$ that the power of the arrived signal is concentrated at the focused

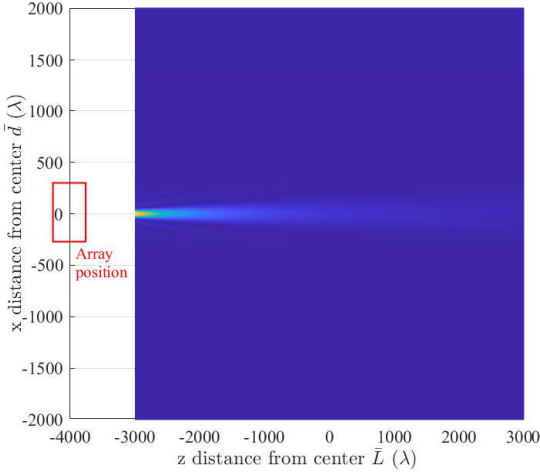


Fig. 9. Power distribution in XoZ plane with $d = 0.5\lambda$

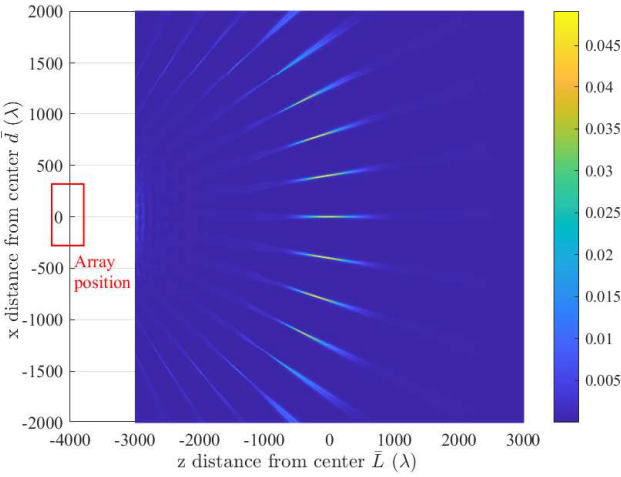


Fig. 10. Power distribution in XoZ plane with $d = 10\lambda$

point along the z -axis. This is because that the phase variation induced by \bar{L} becomes the primary factor influencing the signal power variation.

Fig. 8 further investigates the length of the main lobe in (21) versus the antenna spacing. It indicates that the length of the main lobe decreases rapidly as the antenna spacing increases, especially when the number of antennas N is small. This finding means that sparse arrays can effectively reduce the area of the severe interference region, bringing a potential improvement in system performance. Additionally, it is observed that increasing the number of antennas can also reduce the length of the main lobe.

The simulation results presented in Fig. 5-8 demonstrate a reduction in both the width and length of the main lobe when sparse arrays are employed in near-field XL-MIMO systems. Furthermore, this result is also applicable to the side lobes, since they are caused by the periodic variation of the phase. Therefore, it can be inferred that sparse array XL-MIMO systems can significantly reduce the area of the severe interference region, and bring great system performance in

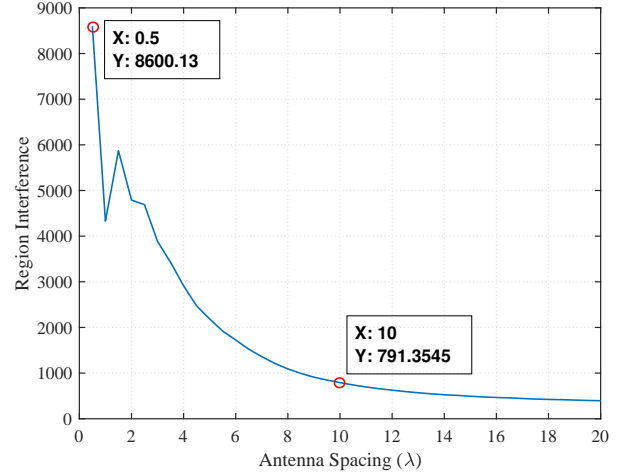


Fig. 11. Region interference versus antenna spacing

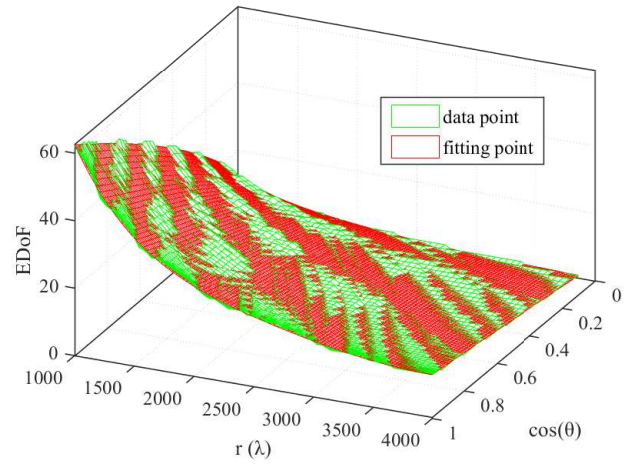


Fig. 12. Result of EDoF function fitting

multi-user scenarios.

Fig. 9 and Fig. 10 respectively exhibits the power distribution of the arrived signal in the XoZ plane with $d = 0.5\lambda$ and $d = 10\lambda$, when the transmit array focuses on the point r_0 . As is observed, for the case with $d = 0.5\lambda$, a wide and long main lobe with strong power is shown in Fig. 9. Meanwhile, for the case with $d = 10\lambda$, we can see many short and narrow lobes with low power. These results are consistent with our previous simulations and theoretical analysis. Additionally, an interesting observation is that when the lobes are grouped based on distance rather than angle, it is found that the sparse array in near-field XL-MIMO systems exhibits only one main lobe in terms of distance.

Furthermore, to figure out the improvement of system performance brought by the sparse array, we perform the simulation in Fig. 11, which shows the region interference versus the antenna spacing. The region interference is calculated by summing up the power of the arrived signal in the XoZ plane, which can represent the inter-user interference in multi-user systems. It is observed that the region interference decreases

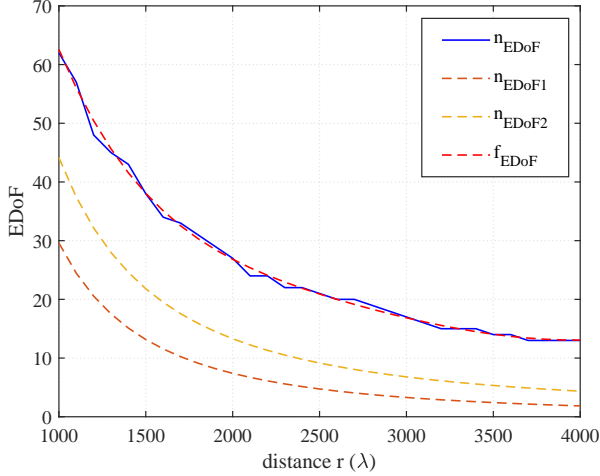


Fig. 13. Different EDoF estimation methods versus r

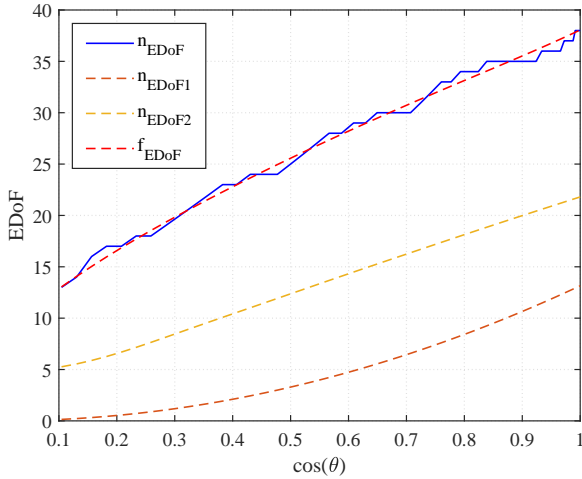


Fig. 14. Different EDoF estimation methods versus $\cos(\theta)$

as the antenna spacing increases. As is shown, the region interference of conventional collected arrays with $d = 0.5\lambda$ is 8600.13, while that of sparse arrays with $d = 10\lambda$ is 791.35. It demonstrates the improvement in system performance with the use of sparse arrays, and this enhancement becomes more pronounced as the antenna spacing increases.

Despite the benefit of reducing the area of the severe interference region, the sparse array offers a critical advantage in significantly enhancing EDoF. In Section IV, we have

proposed Algorithm 2 to obtain a closed-form expression for EDoF with high accuracy using function fitting. The following simulations will introduce an example of obtaining the closed-form expression for EDoF by Algorithm 2 and verify its accuracy.

We assume that the distance between the transmit array and users satisfies $r \in [1000\lambda, 4000\lambda]$, and the deviation angle of users from z_+ -axis satisfies $\theta \in [0, \pi/2 - \pi/30]$. The transmit UPA at the BS is with the size of 35×35 and antenna spacing $d = 10\lambda$. The user is assumed to be in the XoZ plane, equipped with a UPA with the size of 9×9 and $\bar{d} = 2\lambda$. Since the system parameters satisfy $\frac{d\bar{d}\sqrt{N}}{\lambda r_{\min}} < 1$, we can obtain the EDoF fitting function of this case by Algorithm 2 as

$$f_{\text{EDoF}}(\theta, r) = \sum_{i=0}^5 \sum_{j=0}^5 p_{ij} \cos^i(\theta) \left(\frac{r}{\lambda}\right)^j, \quad (22)$$

where the coefficients are given by Table I. Given the EDoF fitting function, Fig. 12 compares the real data point for EDoF obtained by (17) and the fitting point for EDoF obtained by (22). It is observed that the EDoF obtained by the closed-form expression $f_{\text{EDoF}}(\theta, r)$ well matches the real data point, indicating the accuracy of $f_{\text{EDoF}}(\theta, r)$.

In Fig. 13 and Fig. 14, we compare $f_{\text{EDoF}}(\theta, r)$ in (22) with existing EDoF estimation methods as distance r and angle θ vary, respectively. The solid line of n_{EDoF} is obtained by (17), which represents the real EDoF value. The dashed line of n_{EDoF1} is obtained by (18), the dashed line of n_{EDoF2} is based on (18) and the dashed line of f_{EDoF} represents our proposed method $f_{\text{EDoF}}(\theta, r)$. As is observed, the method in (18) has very limited accuracy, while the method in (18) provides a relatively better accuracy. On the other hand, our proposed method provides a highly accurate estimation, significantly outperforming existing estimation methods.

VI. CONCLUSION

We investigated a downlink near-field XL-MIMO communication system with sparse UPAs. Based on the Green's function-based channel model, we focused on the power distribution of the arrived signal near the focused point. In x -axis and y -axis directions, the closed-form expressions for the power distributions were derived in Theorem 1 and Theorem 2, respectively. Based on that, the closed-form expressions for the width and length of the main lobe were derived respectively in (7) and (15), both of which decrease as the antenna spacing increases. Furthermore, we introduced the constraint

TABLE I
COEFFICIENTS OF THE EDoF FITTING FUNCTION

	1	$\left(\frac{r}{\lambda}\right)^1$	$\left(\frac{r}{\lambda}\right)^2$	$\left(\frac{r}{\lambda}\right)^3$	$\left(\frac{r}{\lambda}\right)^4$	$\left(\frac{r}{\lambda}\right)^5$
1	$p_{00} = 63.36$	$p_{01} = -0.1048$	$p_{02} = 8.034 \times 10^{-5}$	$p_{03} = -3.129 \times 10^{-8}$	$p_{04} = 6.014 \times 10^{-12}$	$p_{05} = -4.513 \times 10^{-16}$
$\cos(\theta)$	$p_{10} = 204$	$p_{11} = -0.2026$	$p_{12} = 9.282 \times 10^{-5}$	$p_{13} = -1.957 \times 10^{-8}$	$p_{14} = 1.518 \times 10^{-12}$	$p_{15} = 0$
$\cos^2(\theta)$	$p_{20} = -91.16$	$p_{21} = 0.03111$	$p_{22} = -1.074 \times 10^{-5}$	$p_{23} = 1.609 \times 10^{-9}$	$p_{24} = 0$	$p_{25} = 0$
$\cos^3(\theta)$	$p_{30} = 95.1$	$p_{31} = 0.003449$	$p_{32} = -1.735 \times 10^{-6}$	$p_{33} = 0$	$p_{34} = 0$	$p_{35} = 0$
$\cos^4(\theta)$	$p_{40} = -84.82$	$p_{41} = 0.0008277$	$p_{42} = 0$	$p_{43} = 0$	$p_{44} = 0$	$p_{45} = 0$
$\cos^5(\theta)$	$p_{50} = 29.58$	$p_{51} = 0$	$p_{52} = 0$	$p_{53} = 0$	$p_{54} = 0$	$p_{55} = 0$

(20) on system parameters, under which the EDoF of XL-MIMO systems with sparse UPAs can be precisely estimated. Then, we proposed Algorithm 2 to obtain the EDoF fitting function $f_{\text{EDoF}}(\theta, r)$, which can estimate EDoF with high accuracy and low computational complexity. The numerical results verified the correctness of the main results of this paper. Furthermore, we revealed the improvement in the performance of XL-MIMO systems with the use of sparse arrays, and this enhancement becomes more substantial as the antenna spacing increases.

APPENDIX A PROOF FOR THEOREM 1

When the XL-MIMO array focuses on \mathbf{r}_0 , the received signal f_1 at \mathbf{r}_1 can be expressed as

$$f_1 = \sum_{n=1}^{\sqrt{N}} \sum_{m=1}^{\sqrt{N}} t_{n,m}^1 e^{i\theta_{n,m}^0} s, \quad (23)$$

where $t_{n,m}^1$ is the Green's Function-based channel coefficient between the UPA and \mathbf{r}_1 , given by

$$t_{n,m}^1 = -\frac{\exp\left(ik\left|(\bar{x}_n, \bar{y}_m, 0) - (\bar{d}, 0, L)\right|\right)}{4\pi\left|(\bar{x}_n, \bar{y}_m, 0) - (\bar{d}, 0, L)\right|} \approx -\frac{e^{i\frac{2\pi}{\lambda}\sqrt{\bar{x}_n^2 + \bar{y}_m^2 + L^2 + \bar{d}^2 - 2\bar{x}_n\bar{d}}}}{4\pi L}. \quad (24)$$

Thus, the power of f_1 can be expressed as

$$P_1 = \frac{P}{N} \left| \sum_{n=1}^{\sqrt{N}} \sum_{m=1}^{\sqrt{N}} t_{n,m}^1 e^{i\theta_{n,m}^0} \right|^2 = \frac{P}{(4\pi L)^2} \rho_1, \quad (25)$$

with ρ_1 expressed as

$$\rho_1 = \frac{1}{N} \left| \sum_{n=1}^{\sqrt{N}} \sum_{m=1}^{\sqrt{N}} e^{i\frac{2\pi}{\lambda}\sqrt{\bar{x}_n^2 + \bar{y}_m^2 + L^2 + \bar{d}^2 - 2\bar{x}_n\bar{d}}} e^{i\theta_{n,m}^0} \right|^2. \quad (26)$$

Then, substituting (5) into (26), we further calculate ρ_1 as follows

$$\begin{aligned} \rho_1 &= \frac{1}{N} \left| \sum_{n=1}^{\sqrt{N}} \sum_{m=1}^{\sqrt{N}} e^{i\frac{2\pi}{\lambda}\sqrt{\bar{x}_n^2 + \bar{y}_m^2 + L^2 + \bar{d}^2 - 2\bar{x}_n\bar{d}}} e^{-i\frac{2\pi}{\lambda}\sqrt{\bar{x}_n^2 + \bar{y}_m^2 + L^2}} \right|^2 \\ &\approx \frac{1}{N} \left| \sum_{n=1}^{\sqrt{N}} \sum_{m=1}^{\sqrt{N}} e^{i\frac{2\pi}{\lambda}\left(L + \frac{\bar{x}_n^2}{2L} + \frac{\bar{y}_m^2}{2L} + \frac{\bar{d}^2 - 2\bar{x}_n\bar{d}}{2L}\right)} e^{-i\frac{2\pi}{\lambda}\left(L + \frac{\bar{x}_n^2}{2L} + \frac{\bar{y}_m^2}{2L}\right)} \right|^2 \\ &= \left| \sum_{n=1}^{\sqrt{N}} e^{-i\frac{2\pi}{\lambda}\left(\frac{\bar{d}^2 - 2\bar{x}_n\bar{d}}{2L}\right)} \right|^2 \stackrel{(a)}{=} \left| \sum_{n=1}^{\sqrt{N}} e^{-i\frac{2\pi}{\lambda}\left(\frac{\bar{d}}{2} - \left(n - \frac{\sqrt{N}+1}{2}\right)d\right)\frac{\bar{d}}{L}} \right|^2 \\ &= \left| \sum_{n=1}^{\sqrt{N}} e^{-i\frac{2\pi}{\lambda}\left(\left(n - \frac{\sqrt{N}+1}{2}\right)d - \frac{\bar{d}}{2}\right)\frac{\bar{d}}{L}} \right|^2. \quad (27) \end{aligned}$$

The approximation in (27) is based on the assumption of $L^2 \gg \bar{x}_n^2, \bar{y}_m^2$ and the Taylor approximation $\sqrt{1+x} \approx 1 + \frac{x}{2}$ as $x \rightarrow$

0. Step (a) is obtained by substituting (3) into the expression. Then, the summation term can be derived as

$$\begin{aligned} &\sum_{n=1}^{\sqrt{N}} e^{-i\frac{2\pi}{\lambda}\left(\left(n - \frac{\sqrt{N}+1}{2}\right)d - \frac{\bar{d}}{2}\right)\frac{\bar{d}}{L}} \\ &= \frac{e^{i\frac{2\pi}{\lambda}\left(\frac{\sqrt{N}-1}{2}d + \frac{\bar{d}}{2}\right)\frac{\bar{d}}{L}} \left(1 - e^{-i\frac{2\pi}{\lambda}\frac{\sqrt{N}d\bar{d}}{L}}\right)}{1 - e^{-i\frac{2\pi}{\lambda}\frac{d\bar{d}}{L}}} \\ &= \frac{e^{i\frac{\pi}{\lambda}\left(\bar{d}-d\right)\frac{\bar{d}}{L}} \left(e^{i\frac{2\pi}{\lambda}\left(\frac{\sqrt{N}d}{2}\right)\frac{\bar{d}}{L}} - e^{i\frac{2\pi}{\lambda}\left(-\frac{\sqrt{N}d}{2}\right)\frac{\bar{d}}{L}}\right)}{e^{-i\frac{\pi}{\lambda}d\frac{\bar{d}}{L}} \left(e^{i\frac{\pi}{\lambda}\frac{d\bar{d}}{L}} - e^{-i\frac{\pi}{\lambda}\frac{d\bar{d}}{L}}\right)} \\ &= \frac{e^{i\frac{\pi}{\lambda}\frac{\bar{d}^2}{L}} 2i \sin\left(\frac{2\pi}{\lambda}\left(\frac{\sqrt{N}d}{2}\right)\frac{\bar{d}}{L}\right)}{2i \sin\left(\frac{\pi}{\lambda}\frac{d\bar{d}}{L}\right)} = e^{i\frac{\pi d^2}{\lambda L}} \frac{\sqrt{N} \sin c\left(\frac{\sqrt{N}d^2}{\lambda L}\right)}{\sin c\left(\frac{d^2}{\lambda L}\right)}. \quad (28) \end{aligned}$$

Substituting (28) and (27) into (25), we finish the proof for Theorem 1.

APPENDIX B PROOF FOR THEOREM 2

When the XL-MIMO array focuses on \mathbf{r}_0 , the received signal f_2 at \mathbf{r}_2 can be expressed as

$$f_2 = \sum_{n=1}^{\sqrt{N}} \sum_{m=1}^{\sqrt{N}} t_{n,m}^2 e^{i\theta_{n,m}^0} s, \quad (29)$$

where $t_{n,m}^2$ is the Green's Function-based channel coefficient between the UPA and \mathbf{r}_2 , given by

$$t_{n,m}^2 = -\frac{\exp\left(ik\left|(\bar{x}_n, \bar{y}_m, 0) - (0, 0, L + \bar{L})\right|\right)}{4\pi\left|(\bar{x}_n, \bar{y}_m, 0) - (0, 0, L + \bar{L})\right|} \approx -\frac{\exp\left(i\frac{2\pi}{\lambda}\sqrt{\bar{x}_n^2 + \bar{y}_m^2 + (L + \bar{L})^2}\right)}{4\pi(L + \bar{L})}. \quad (30)$$

Thus, the power of f_2 can be expressed as

$$P_2 = \frac{P}{N} \left| \sum_{n=1}^{\sqrt{N}} \sum_{m=1}^{\sqrt{N}} t_{n,m}^2 e^{i\theta_{n,m}^0} \right|^2 = \frac{P}{(4\pi(L + \bar{L}))^2} \rho_2, \quad (31)$$

with ρ_2 expressed as

$$\rho_2 = \frac{1}{N} \left| \sum_{n=1}^{\sqrt{N}} \sum_{m=1}^{\sqrt{N}} e^{i\frac{2\pi}{\lambda}\sqrt{\bar{x}_n^2 + \bar{y}_m^2 + (L + \bar{L})^2}} e^{i\theta_{n,m}^0} \right|^2. \quad (32)$$

Then, from (3) and (5), we can calculate ρ_2 as follows

$$\begin{aligned} \rho_2 &= \frac{1}{N} \left| \sum_{n=1}^{\sqrt{N}} \sum_{m=1}^{\sqrt{N}} e^{i\frac{2\pi}{\lambda}\sqrt{\bar{x}_n^2 + \bar{y}_m^2 + (L + \bar{L})^2}} e^{-i\frac{2\pi}{\lambda}\sqrt{\bar{x}_n^2 + \bar{y}_m^2 + L^2}} \right|^2 \\ &\approx \frac{1}{N} \left| \sum_{n=1}^{\sqrt{N}} \sum_{m=1}^{\sqrt{N}} e^{i\frac{2\pi}{\lambda}\left((L + \bar{L}) + \frac{\bar{x}_n^2}{2(L + \bar{L})} + \frac{\bar{y}_m^2}{2(L + \bar{L})}\right)} e^{-i\frac{2\pi}{\lambda}\left(L + \frac{\bar{x}_n^2}{2L} + \frac{\bar{y}_m^2}{2L}\right)} \right|^2 \end{aligned}$$

$$\begin{aligned}
&= \frac{1}{N} \left| \sum_{n=1}^{\sqrt{N}} \sum_{m=1}^{\sqrt{N}} e^{-i\frac{\pi}{\lambda} \frac{\bar{L}d^2(n^2+m^2-(\sqrt{N}+1)(n+m)+\frac{N+2\sqrt{N}+1}{2})}{L(L+\bar{L})}} \right|^2 \\
&= \frac{1}{N} \left| \sum_{n=1}^{\sqrt{N}} \sum_{m=1}^{\sqrt{N}} e^{-i\frac{\pi}{\lambda} \frac{\bar{L}d^2(n(n-\sqrt{N}-1)+m(m-\sqrt{N}-1))}{L(L+\bar{L})}} \right|^2 \\
&= \frac{1}{N} \left| \sum_{n=1}^{\sqrt{N}} e^{-i\frac{\pi}{\lambda} \frac{\bar{L}d^2n(n-\sqrt{N}-1)}{L(L+\bar{L})}} \sum_{m=1}^{\sqrt{N}} e^{-i\frac{\pi}{\lambda} \frac{\bar{L}d^2m(m-\sqrt{N}-1)}{L(L+\bar{L})}} \right|^2 \\
&= \frac{1}{N} \left| \sum_{n=1}^{\sqrt{N}} e^{-i\frac{\pi}{\lambda} \frac{\bar{L}d^2n(n-\sqrt{N}-1)}{L(L+\bar{L})}} \right|^4. \tag{33}
\end{aligned}$$

The approximation in (33) is based on the assumption of $(L + \bar{L})^2 \gg \bar{x}_n^2, \bar{y}_m^2$ and the Taylor approximation $\sqrt{1+x} \approx 1 + \frac{x}{2}$ as $x \rightarrow 0$.

Note that

$$\begin{aligned}
&\left| \sum_{n=1}^{\sqrt{N}} e^{-i\frac{\pi}{\lambda} \frac{\bar{L}d^2n(n-\sqrt{N}-1)}{L(L+\bar{L})}} \right| \\
&\stackrel{(a)}{=} \left| \sum_{n'=1-\frac{\sqrt{N}}{2}}^{\frac{\sqrt{N}-1}{2}} e^{-i\frac{\pi}{\lambda} \frac{\bar{L}d^2(n'+\frac{\sqrt{N}+1}{2})(n'-\frac{\sqrt{N}+1}{2})}{L(L+\bar{L})}} \right| \\
&\stackrel{(b)}{=} \left| \sum_{n=1-\frac{\sqrt{N}}{2}}^{\frac{\sqrt{N}-1}{2}} e^{-i\frac{\pi}{\lambda} \frac{\bar{L}d^2(n+\frac{\sqrt{N}+1}{2})(n-\frac{\sqrt{N}+1}{2})}{L(L+\bar{L})}} \right| \\
&= \left| e^{i\frac{\pi}{\lambda} \frac{\bar{L}d^2(\frac{\sqrt{N}+1}{2})^2}{L(L+\bar{L})}} \sum_{n=1-\frac{\sqrt{N}}{2}}^{\frac{\sqrt{N}-1}{2}} e^{-i\frac{\pi}{\lambda} \frac{\bar{L}d^2n^2}{L(L+\bar{L})}} \right| \\
&= \left| \sum_{n=1-\frac{\sqrt{N}}{2}}^{\frac{\sqrt{N}-1}{2}} e^{-i\frac{\pi d^2 n^2}{\lambda L} \frac{\bar{L}}{(L+\bar{L})}} \right|, \tag{34}
\end{aligned}$$

where step (a) is based on $n = n' + \frac{\sqrt{N}+1}{2}$, and step (b) is to replace notation n' by n . Thus, ρ_2 can be further expressed as

$$\rho_2 = \frac{1}{N} \left| \sum_{n=1-\frac{\sqrt{N}}{2}}^{\frac{\sqrt{N}-1}{2}} e^{-i\frac{\pi d^2 n^2}{\lambda L} \frac{\bar{L}}{(L+\bar{L})}} \right|^4 = \frac{1}{N} |\varepsilon|^4, \tag{35}$$

with ε defined as

$$\begin{aligned}
\varepsilon &\triangleq \sum_{n=1-\frac{\sqrt{N}}{2}}^{\frac{\sqrt{N}-1}{2}} e^{-iA\eta n^2}, \\
A &= \frac{\pi d^2}{\lambda L}, \\
\eta &= \frac{\bar{L}}{L + \bar{L}}. \tag{36}
\end{aligned}$$

To further investigate the properties of ρ_2 , we approximate ε using Euler-Maclaurin formula, which is a method for approximating summation terms by transforming the summation into

an integral, thereby simplifying the calculation [29]. Then, we have

$$\varepsilon \approx \int_{\frac{1-\sqrt{N}}{2}}^{\frac{\sqrt{N}-1}{2}} e^{-iA\eta x^2} dx, \tag{37}$$

which can be further expressed as

$$\begin{aligned}
\varepsilon &= \int_{\frac{1-\sqrt{N}}{2}}^{\frac{\sqrt{N}-1}{2}} \cos(A\eta x^2) dx - i \int_{\frac{1-\sqrt{N}}{2}}^{\frac{\sqrt{N}-1}{2}} \sin(A\eta x^2) dx \\
&\stackrel{t=\sqrt{A\eta}x, \eta>0}{=} \frac{1}{\sqrt{A\eta}} \int_{\sqrt{A\eta} \cdot \frac{1-\sqrt{N}}{2}}^{\sqrt{A\eta} \cdot \frac{\sqrt{N}-1}{2}} \cos(t^2) dt \\
&\quad - \frac{1}{\sqrt{A\eta}} \int_{\sqrt{A\eta} \cdot \frac{1-\sqrt{N}}{2}}^{\sqrt{A\eta} \cdot \frac{\sqrt{N}-1}{2}} \sin(t^2) dt \\
&= \frac{1}{\sqrt{A\eta}} [C(b) - C(-b) - i(S(b) - S(-b))] \\
&= \frac{2}{\sqrt{A\eta}} [C(b) - iS(b)], \tag{38}
\end{aligned}$$

where functions $C(\cdot)$ and $S(\cdot)$ are Fresnel integrals, respectively given by (12). Parameter b is defined as

$$b = \sqrt{|A\eta|} \cdot \frac{\sqrt{N}-1}{2}. \tag{39}$$

It is noted that Eq. (38) analyzes the case of $\eta > 0$. For the case of $\eta < 0$, we can use the similar method. Thus, ε can be expressed as

$$\varepsilon = \begin{cases} \frac{2}{\sqrt{|A\eta|}} [C(b) - iS(b)], & \eta \neq 0 \\ \sqrt{N}-1, & \eta = 0 \end{cases}. \tag{40}$$

Substituting (40) into (35), we complete the proof for Theorem 2.

APPENDIX C PROOF FOR COROLLARY 1

According to the definition of b in (11), it is readily observed that b has the range of $[0, +\infty)$. Then, by differentiating ρ_2 , we investigate the monotonicity of ρ_2 in the vicinity of $b = 0^+$.

When $b > 0$, ρ_2 can be re-expressed as

$$\rho_2 = \frac{(\sqrt{N}-1)^4}{N} f(b) g(b), \tag{41}$$

where we define

$$f(b) = \frac{1}{b^4}, \tag{42}$$

$$g(b) = (C^2(b) + S^2(b))^2. \tag{43}$$

Then, the derivative of ρ_2 is calculated as

$$\frac{d\rho_2}{db} = \frac{(\sqrt{N}-1)^4}{N} \left[\frac{d}{db} (f(b) g(b)) + f(b) \frac{d}{db} (g(b)) \right]. \tag{44}$$

The derivative of $f(b)$ is expressed as

$$\frac{d}{db} (f(b)) = \frac{d}{db} \left(\frac{1}{b^4} \right) = -\frac{4}{b^5}. \tag{45}$$

The derivative of $g(b)$ is obtained as

$$\begin{aligned} \frac{d}{db}(g(b)) &= \frac{d}{db} \left((C^2(b) + S^2(b))^2 \right) \\ &= 2(C^2(b) + S^2(b)) \cdot 2 \left(C(b) \cdot \frac{dC}{db} + S(b) \cdot \frac{dS}{db} \right) \\ &= 4(C^2(b) + S^2(b)) \left(C(b) \cos\left(\frac{\pi}{2}b^2\right) + S(b) \sin\left(\frac{\pi}{2}b^2\right) \right). \end{aligned} \quad (46)$$

Substituting (45) and (46) into (44), we obtain the derivative of ρ_2 as

$$\begin{aligned} \frac{d\rho_2}{db} &= \frac{4(\sqrt{N}-1)^4}{Nb^4} (C^2(b) + S^2(b)) \times \\ &\left[-\frac{1}{b}(C^2(b) + S^2(b)) + \left(C(b) \cos\left(\frac{\pi}{2}b^2\right) + S(b) \sin\left(\frac{\pi}{2}b^2\right) \right) \right]. \end{aligned} \quad (47)$$

It is noted from (47) that the sign of $\frac{d\rho_2}{db}$ depends on the following two terms

$$\text{term1} = -\frac{1}{b}(C^2(b) + S^2(b)), \quad (48)$$

$$\text{term2} = C(b) \cos\left(\frac{\pi}{2}b^2\right) + S(b) \sin\left(\frac{\pi}{2}b^2\right). \quad (49)$$

When b is close to 0, term1 dominates the sign of $\frac{d\rho_2}{db}$, since the factor of $\frac{1}{b}$ makes the absolute value of term1 very large. In this case, ρ_2 decreases rapidly and monotonically with b , since term1 < 0 . When b becomes large, the absolute value of term1 drops off, and thus term2 dominates the sign of $\frac{d\rho_2}{db}$, which is a function of b with finite oscillations, alternating between positive and negative values. This characteristic decides that ρ_2 fluctuates within a limited range as b grows.

By analyzing the characteristic of ρ_2 with its derivative $\frac{d\rho_2}{db}$, we complete the proof for Corollary 1.

REFERENCES

- [1] F. Rusek, D. Persson, B. K. Lau, E. G. Larsson, T. L. Marzetta, O. Edfors, and F. Tufvesson, "Scaling up MIMO: Opportunities and challenges with very large arrays," *IEEE Signal Process. Mag.*, vol. 30, no. 1, pp. 40–60, Jan. 2013.
- [2] H. Q. Ngo, E. G. Larsson, and T. L. Marzetta, "Energy and spectral efficiency of very large multiuser MIMO systems," *IEEE Trans. Commun.*, vol. 61, no. 4, pp. 1436–1449, Apr. 2013.
- [3] E. G. Larsson, O. Edfors, F. Tufvesson, and T. L. Marzetta, "Massive MIMO for next generation wireless systems," *IEEE Commun. Mag.*, vol. 52, no. 2, pp. 186–195, Feb. 2014.
- [4] T. L. Marzetta, E. G. Larsson, H. Yang, and H. Q. Ngo, *Fundamentals of Massive MIMO*. Cambridge University Press, 2016.
- [5] L. Sanguinetti, E. Björnson, and J. Hoydis, "Toward massive MIMO 2.0: Understanding spatial correlation, interference suppression, and pilot contamination," *IEEE Trans. Commun.*, vol. 68, no. 1, pp. 232–257, Jan. 2020.
- [6] E. Björnson, L. Sanguinetti, H. Wymeersch, J. Hoydis, and T. L. Marzetta, "Massive MIMO is a reality—what is next?: Five promising research directions for antenna arrays," *Digital Signal Process.*, vol. 94, pp. 3–20, Nov. 2019.
- [7] Z. Zhang, Y. Xiao, Z. Ma, M. Xiao, Z. Ding, X. Lei, G. K. Karagiannidis, and P. Fan, "6G wireless networks: Vision, requirements, architecture, and key technologies," *IEEE Veh. Technol. Mag.*, vol. 14, no. 3, pp. 28–41, Sep. 2019.
- [8] Z. Wang, J. Zhang, H. Du, W. E. I. Sha, B. Ai, D. Niyato, and M. Debbah, "Extremely large-scale MIMO: Fundamentals, challenges, solutions, and future directions," *IEEE Wireless Commun.*, vol. 31, no. 3, pp. 117–124, Jun. 2024.
- [9] H. Lu, Y. Zeng, C. You, Y. Han, J. Zhang, Z. Wang, Z. Dong, S. Jin, C.-X. Wang, T. Jiang, X. You, and R. Zhang, "A tutorial on near-field XL-MIMO communications towards 6G," *IEEE Commun. Surveys Tuts.*, Apr. 2024, early access.
- [10] E. D. Carvalho, A. Ali, A. Amiri, M. Angelichinoski, and R. W. Heath, "Non-stationarities in extra-large-scale massive MIMO," *IEEE Wireless Commun.*, vol. 27, no. 4, pp. 74–80, Aug. 2020.
- [11] H. Lu and Y. Zeng, "Communicating with extremely large-scale array/surface: Unified modeling and performance analysis," *IEEE Trans. Wireless Commun.*, vol. 21, no. 6, pp. 4039–4053, Jun. 2022.
- [12] K. Zhi, C. Pan, H. Ren, K. K. Chai, C.-X. Wang, R. Schober, and X. You, "Performance analysis and low-complexity design for XL-MIMO with near-field spatial non-stationarities," *IEEE J. Sel. Areas Commun.*, vol. 42, no. 6, pp. 1656–1672, Jun. 2024.
- [13] M. Liu, C. Pan, K. Zhi, H. Ren, and J. Wang, "Hybrid precoding design for near-field wideband thz systems with spatial non-stationarity," *IEEE Commun. Lett.*, vol. 28, no. 10, pp. 2372–2376, Oct. 2024.
- [14] L. Liu, W. Hong, H. Wang, G. Yang, N. Zhang, H. Zhao, J. Chang, C. Yu, X. Yu, H. Tang, H. Zhu, and L. Tian, "Characterization of line-of-sight MIMO channel for fixed wireless communications," *IEEE Antennas Wireless Propag. Lett.*, vol. 6, pp. 36–39, Dec. 2007.
- [15] G. J. Foschini and M. J. Gans, "On limits of wireless communications in a fading environment when using multiple antennas," *Wireless Pers. Commun.*, vol. 6, no. 3, pp. 311–335, Mar. 1998.
- [16] D. A. B. Miller, "Waves, modes, communications, and optics: a tutorial," *Adv. Opt. Photon.*, vol. 11, no. 3, pp. 679–825, 2019.
- [17] D. Dardari, "Communicating with large intelligent surfaces: Fundamental limits and models," *IEEE J. Sel. Areas Commun.*, vol. 38, no. 11, pp. 2526–2537, Jul. 2020.
- [18] Z. Wu, M. Cui, Z. Zhang, and L. Dai, "Distance-aware precoding for near-field capacity improvement in XL-MIMO," in *2022 IEEE 95th Veh. Technol. Conf. (VTC-Spring)*, Jun. 2022, pp. 1–5.
- [19] S. S. A. Yuan, Z. He, X. Chen, C. Huang, and W. E. I. Sha, "Electromagnetic effective degree of freedom of an MIMO system in free space," *IEEE Antennas and Wireless Propag. Lett.*, vol. 21, no. 3, pp. 446–450, Mar. 2022.
- [20] Z. Wang, J. Zhang, W. Yi, H. Du, D. Niyato, B. Ai, and D. W. K. Ng, "Analytical framework for effective degrees of freedom in near-field XL-MIMO," 2024. [Online]. Available: <https://arxiv.org/abs/2401.15280>
- [21] X. Chen, H. Ren, C. Pan, Z. Peng, and J. Wang, "Effective DoF-oriented optimal antenna spacing in near-field XL-MIMO systems," 2025. [Online]. Available: <https://arxiv.org/abs/2501.07062>
- [22] C. I. Coman, I. E. Lager, and L. P. Ligthart, "Design considerations in sparse array antennas," in *Proc. Eur. Radar Conf.*, Sep. 2006, pp. 72–75.
- [23] D. Kurup, M. Himdi, and A. Rydberg, "Synthesis of uniform amplitude unequally spaced antenna arrays using the differential evolution algorithm," *IEEE Trans. Antennas Propag.*, vol. 51, no. 9, pp. 2210–2217, Sep. 2003.
- [24] Y. V. Krivosheev and A. V. Shishlov, "Grating lobe suppression in phased arrays composed of identical or similar subarrays," in *Proc. IEEE Int. Symp. Phased Array Syst. Technol.*, Oct. 2010, pp. 724–730.
- [25] Z. Gao, Z. Wan, D. Zheng, S. Tan, C. Masouros, D. W. K. Ng, and S. Chen, "Integrated sensing and communication with mmwave massive MIMO: A compressed sampling perspective," *IEEE Trans. Wireless Commun.*, vol. 22, no. 3, pp. 1745–1762, Mar. 2023.
- [26] H. Wang and Y. Zeng, "Can sparse arrays outperform collocated arrays for future wireless communications?" in *Proc. IEEE GLOBECOM Workshops (GC Wkshps)*, 2023, pp. 667–672.
- [27] X. Li, Z. Dong, Y. Zeng, S. Jin, and R. Zhang, "Multi-user modular XL-MIMO communications: Near-field beam focusing pattern and user grouping," *IEEE Trans. Wireless Commun.*, vol. 23, no. 10, pp. 13766–13781, Oct. 2024.
- [28] B. Emil, C. Chan-Byoung, W. H. J. a. Robert, L. M. Thomas, M. Amine, S. Luca, R. Fredrik, R. C. Miguel, J. Dongsoo, and T. D. Özlem, "Towards 6G MIMO: Massive spatial multiplexing, dense arrays, and interplay between electromagnetics and processing," 2024. [Online]. Available: <https://arxiv.org/abs/2401.02844>
- [29] C. M. Bender and S. A. Orszag, *Advanced Mathematical Methods For Scientists And Engineers*. Advanced Mathematical Methods for Scientists and Engineers I, 1999.